AIAA JOURNAL
Vol. 39, No. 10, October 2001

Validation of Computed High-Lift Flows with Significant Wind-Tunnel Effects

Stuart E. Rogers* and Karlin Roth†
NASA Ames Research Center, Moffett Field, California 94035
and
Steven M. Nash‡
MCAT, Inc., Moffett Field, California 94035

The modeling requirements for validating Navier–Stokes computations of a high-lift trapezoidal wing are investigated. This wing has a full-span slat and a full-span flap and has been tested extensively in the NASA Langley 14 × 22-ft Wind Tunnel and the NASA Ames 12-ft Pressure Wind Tunnel. Because of the size of the wing, there are significant facility effects in the data from the 12-ft wind tunnel. Computational models of the test facility of differing fidelity are developed and tested. Results are compared with experimental lift, drag, and surface pressures. In the computations a simplified, inviscid model of the test section performs as well as a high-fidelity, viscous test-section model. Computed results generally compare very well with experimental data at all but the highest angles of attack. A comparison of computational results from both free-air and wind-tunnel simulations at the same lift condition indicates that it is necessary to simulate the wind tunnel to perform validation using the 12-ft wind-tunnel experimental data. A subsequent grid-refinement study found that enhanced spanwise resolution increased the accuracy of the computed surface pressures at high angle of attack and resulted in a computed maximum lift that was 5% above the experimental value.

Introduction

VALIDATION of computational fluid dynamics (CFD) software is a very important part of its development cycle. It is also an ongoing process for the life of the software. A general-purpose CFD solver can be used for a wide range of fluid-flow problems. Validation of the solver for a simple problem, such as attached flow over an airfoil, does not validate the software for a difficult problem, such as the flow over a complete aircraft. Thus, responsible use of the software for solving a new class of flow problems requires validation. The current work is part of a validation effort for the flow over complex high-lift configurations using an overset grid approach[1–3] and the OVERFLOW solver.[4,5]

Calculating the viscous fluid flow over high-lift configurations challenges CFD. Even in two dimensions, state-of-the-art CFD codes fail to consistently predict, with sufficient accuracy, trends with Reynolds number or trends with flap/slat rigging changes.[6] The difficulties in simulating high-lift flows come from the severe complexity of both the geometry and the flowfield physics. In particular, the wing has multiple elements with very small gaps between them, leading to an interaction of various viscous flow phenomena.[7] Because the fluid dynamics are dominated by viscous effects, only a high-fidelity simulation using the Navier–Stokes equations can provide the accuracy necessary to assist in aircraft design.

Only a limited amount of validation has been performed in the past for three-dimensional high-lift flows. Some of the reasons given by Bussoletti et al.[8] for the lack of such validations include a lack of sufficient three-dimensional experimental high-lift data; only a limited number of three-dimensional high-lift simulations had been conducted, and the available simulations had been done on relatively simple geometries; such simulations required significant computational and labor resources; and most viscous computational approaches were not able to simulate the complex geometries found on an aircraft configured for high lift.

Previous high-lift CFD simulations and validation in three-dimensions include Mathias et al.[9] and Jones et al.,[10] who studied a simple wing with a half-span flap; Cao et al.[11] who computed flow over a simplified Boeing 747 high-lift configuration; Mavriplis[12,13] and Nash and Rogers,[14] who computed flow over the same high-lift trapezoidal wing used in the current work. Some work performed during the same time period as the present work on some complete high-lift aircraft simulations is reported by Slotnick et al.[15] and by Rogers et al.[16] In all of these works, the validation was limited to comparisons with experimental forces and pressure coefficients. In some of these works,[9,15] the high-lift configurations were simulated within the wind tunnel, whereas in the others the configurations were simulated only in free air.

High-lift configurations generate more lift than cruise configurations, and they experience maximum lift at much higher angles of attack. Because of this, the wall-interference corrections for experimental data acquired for high-lift configurations can be large and thus of questionable accuracy. Testing with smaller models would reduce the amount of interference, but the overruling need for higher Reynolds numbers forces the experimentalists to test with larger models. The present study compares OVERFLOW simulations of the flow over a trapezoidal high-lift wing (trap wing) with recently acquired experimental data.[17] This wing has been tested in both the NASA Langley 14- × 22-ft Wind Tunnel (14 × 22 tunnel) and the NASA Ames 12-ft Pressure Wind Tunnel (12-ft tunnel). The blockage area for the trap wing at 26 deg angle of attack in the 12-ft tunnel test section is 10% of the test-section area. Further, for this configuration interference correction methods indicate a change of over six degrees in angle of attack caused by the 12-ft tunnel facility walls. Thus, the primary goal of the current work is to determine if it is necessary to model the wind-tunnel walls in order to use the 12-ft tunnel data for CFD validation of flow over the trap wing.

Numerous authors have reported on efforts to simulate wind-tunnel facilities in their CFD calculations. Much of the research in this area has focused on developing boundary conditions to simulate porous or slotted wind-tunnel walls, examples of which are

Received 13 July 2000; presented as Paper 2000-4218 at the AIAA 18th Applied Aerodynamics Conference, Denver, CO, 14–17 August 2000; revision received 11 April 2001; accepted for publication 16 April 2001.

*Aerospace Engineer, Mail Stop T27B-1, NAS Systems Division; rogers@nas.nasa.gov. Senior Member AIAA.
†Chief, Aerospace Operations Modeling Office, Mail Stop 210-10; kroth@mail.arc.nasa.gov. Senior Member AIAA.
‡Research Engineer; currently Software Engineer, System Products, Sun Microsystems, Inc., 901 San Antonio Road, VMPK27-301, Palo Alto, CA 94304-4900; steve.nash@eng.sun.com.

given in Refs. 18–21. Although much of this work was focused on airfoils in transonic flows with relatively small blockage, the current issues are more concerned with large blockage in a three-dimensional semispan testing environment. Of interest to high lift is the work by Cao et al.,[22] who studied the effects of upper and lower wind-tunnel walls while computing a high-lift airfoil configuration. They investigated the use of both inviscid and viscous boundary conditions on the walls and found very little difference between the two. They reported nonnegligible interference effects when comparing the wind-tunnel wall computations with free-air computations. A direct predecessor to the current work is that of Djomehri,[23] who performed a preliminary investigation of computing flow through the 12-ft tunnel, using both viscous and inviscid surfaces to model the wind tunnel.

In the following sections details of the trap-wing geometry used in this study are presented. Following this is a presentation of the computational grids, which were generated for this work, including both a viscous-surface, high-fidelity representation of the 12-ft tunnel, as well as a simplified model of the test section. The computed results are presented, including detailed comparisons between the computed and experimental data and an analysis of the wind-tunnel interference. Finally, results of computations from a second computational grid with refined spanwise spacing are presented.

Trap-Wing and Wind-Tunnel Geometries

Experimental Model

Recent experimental work on a high-lift trap-wing configuration[17] was motivated by the need to produce data that could be used to validate CFD methods for realistic three-dimensional high-lift flows. This trap-wing configuration is a semispan model and consists of a body pod, a wing, a full-span slat, and either a full-span or a part-span flap. The current work focuses on the full-span flap configuration. The model has been tested in both the 14×22 tunnel and the 12-ft tunnel. The 12-ft tunnel data were taken at Reynolds numbers, based on mean aerodynamic chord (Re_c) from 3.4×10^6 to 14.7×10^6 (1–4.3 atm), with a Mach number of 0.15; the 14×22 tunnel data were taken at $Re_c = 4.3 \times 10^6$ and a Mach number of 0.2. The data taken in the 12-ft tunnel included forces and moments, surface pressures, off-body and wake velocity profiles measured with a seven-hole probe, transition measurements using temperature sensitive paint, minituft surface flow visualization, and wind-tunnel wall pressures. The mean aerodynamic chord c of the model was 39.6 in. (100.6 cm), and the model semispan was 85 in. (215.9 cm). All of the current computed results were obtained for trap-wing landing configuration number one, which had slat and flap deflections of 30 and 25 deg, respectively, a slat gap of $0.015c$, slat overhang of $0.015c$, a flap gap of $0.015c$, and a flap overhang of $0.005c$. In the 12-ft tunnel the model was mounted on a splitter plate above the floor of the wind tunnel, as seen in Fig. 1.

Wind-Tunnel Interference

Some initial CFD results for this geometry have been compared to the lower-Reynolds-number data from the 14×22 tunnel in a previous work by the current authors.[14] These results compared very well with the 14×22 tunnel experimental data: the computed lift coefficient $\boldsymbol{C}_L$ varied from the experimental data by no more then 1.5% from a low angle of attack α through maximum lift coefficient $\boldsymbol{C}_{L,\max}$. Figure 2 is a plot of $\boldsymbol{C}_L$ vs α comparing the 12-ft tunnel data, ($Re_c = 5.9 \times 10^6$, Mach = 0.15), corrected and uncorrected, with the 14×22 tunnel corrected data ($Re_c = 4.3 \times 10^6$, Mach = 0.2). Also included in Fig. 2 are previously computed CFD results,[14] which were run at the flow conditions of the 14×22 tunnel and using free-air boundary conditions. This shows that the blockage in the 12-ft tunnel is very high, with a shift of up to 6 deg in angle of attack between the corrected and uncorrected $\boldsymbol{C}_L$.

Because the 14×22 tunnel test section is considerably larger than that of the 12-ft tunnel, the corrections to the 14×22 tunnel data are much smaller. This is supported by the excellent agreement between the 14×22 tunnel data and the free-air CFD results. Although the corrected data from the two wind tunnels agree fairly well at the lower angles of attack, the corrected 12-ft tunnel $\boldsymbol{C}_{L,\max}$ is considerably lower. The higher Reynolds number and the lower

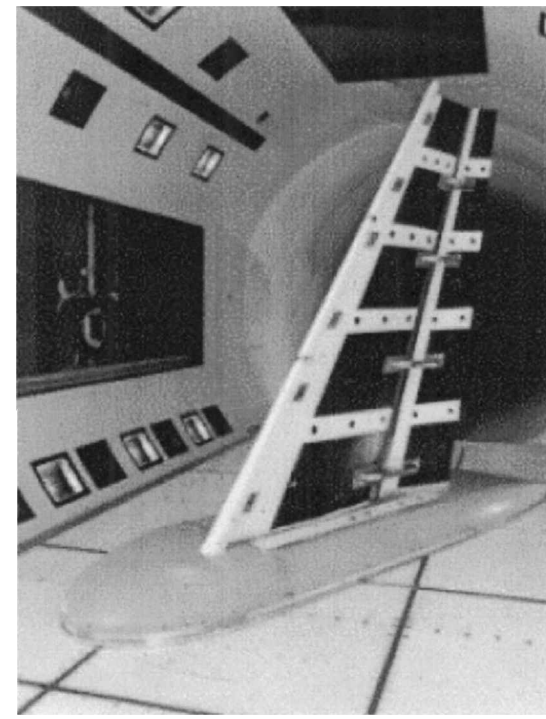

Fig. 1 Trap wing in the 12-ft tunnel test section.

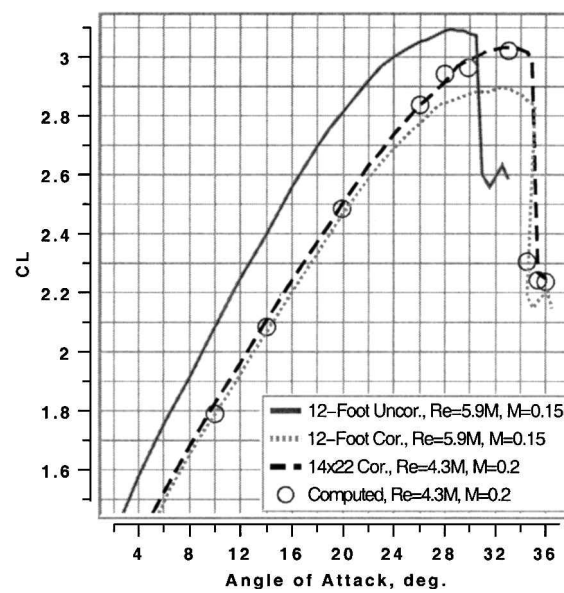

Fig. 2 C_L vs α comparing 12-ft tunnel and 14 × 22 tunnel data.

Mach number of the 12-ft tunnel data should both tend to produce higher $\boldsymbol{C}_{L,\max}$ values. Thus the difference in the $\boldsymbol{C}_{L,\max}$ values is likely caused by a difference between the two facilities. The conclusion drawn from Fig. 2 is that any CFD comparisons with the 12-ft tunnel trap-wing data should simulate the effects of the test section and should be validated with the uncorrected data. This conclusion is strongly endorsed by the experimental investigators.[17]

Computational Model

The computational model of the trap wing includes all components of the experimental model except the brackets that hold the slat and flap elements onto the wing. The grid generation starts with the geometry as defined in CAD files supplied by the trap-wing experimental-design team. The trap-wing grid system is generated utilizing the Chimera Grid Tools[24] (data also available online at http://www.nas.nasa.gov/~rogers/cgt/doc/man.html), which include a series of general-purpose scripts, enabling rapid grid-generation and configuration control.[3] The inboard ends of the slat,

wing, and flap are sealed against the body pod using collar grids[25] at the intersections. At the tips of these three elements, wing-cap grids[2] are used. Figure 3 shows these wing-cap surface grids with only every other grid line plotted.

In the present computational work, the 12-ft tunnel test section was modeled using two different approaches. The first of these was a high-fidelity model that included all components present in the 12-ft tunnel test section. This included a horizontal splitter plate above the tunnel floor on which the model is mounted, a large center fairing underneath the splitter plate; and four hinge fairings at the underside trailing edge of the splitter plate. These features are shown in Figs. 4 and 5. Figure 4 is a schematic view of the 12-ft tunnel test section with the trap-wing model in place. The definition of the wind-tunnel walls used in the computational grid included the slight divergence of the test section to accommodate the boundary-layer growth. The complete model treated all of the solid surfaces as no-slip, viscous surfaces, and this model is referred to as the "viscous tunnel model." The grid surfaces of the viscous-tunnel model are shown in Fig. 5, in which only every fourth grid line is drawn. This complete test-section model adds over 8.3 million grid points to the trap-wing grid system. With the viscous model of the 12-ft tunnel, the entire trap-wing grid system consists of 14.4 million grid points and 36 zones.

To mount the trap wing in the viscous-tunnel model, the body pod was given a 1-in. (2.54-cm) standoff above the splitter plate. This standoff distance was sealed with a viscous collar grid grown onto both the body pod and the splitter plate. In the experiment a labyrinth seal was used with a standoff height of approximately 1 in. (2.54 cm).

In the viscous-tunnel model the inflow region upstream of the test section included only part of the bell mouth from the actual tunnel. The computational inflow region was built from a constant-area, circular cross section, which was faired into the downstream section of the actual bell mouth. This was done to reduce the inflow cross-section area and thus avoid computing an inflow region with very small-magnitude velocities. The outflow region of the computational domain was built by blending together a constant-area cross section with the actual tunnel geometry, starting about 200 in. (508 cm) downstream of the trailing edge of the splitter plate. If the actual wind-tunnel outflow expansion was used, it was found that the wakes generated by the high-lift test articles and the wind-tunnel wall boundary layer would separate and become unsteady through the adverse-pressure gradient of the expansion. This unsteady separation would affect the entire flowfield, which would never converge to a steady state. The use of a constant-area outflow section eliminated this behavior.

Because of the cost of using such a high-fidelity representation of the test section, a simpler computational model was also developed. This model consisted of a constant cross-section tube, whose surfaces were treated with inviscid boundary conditions. The cross section of the tube matched only the cross section of the actual test section above the splitter plate at the model reference location. This model of the test section was generated using two zones and required 1.2 million grid points. Utilizing this inviscid model of the 12-ft tunnel, the entire grid system for the trap wing was composed of 14 zones and 6.8 million grid points. Figure 6 shows the surface grids on the entire configuration inside the inviscid wind-tunnel grid, mounted at 26-deg angle of attack. For clarity, only every fourth grid point in each computational direction is plotted in Fig. 6.

In addition to the two wind-tunnel grid systems, a free-air grid system was generated by utilizing several Cartesian grids, which extended to the far field. The entire free-air grid system contains 6.0 million grid points and 15 zones.

When a model of the wind-tunnel walls was included in the computations, the grid system had to be regenerated for each angle of attack. This was a straightforward task with the overset grid approach. This process started by generating all of the body-fitted volume grids attached to the trap-wing components. These same trap-wing grids are used for both wind-tunnel models and for the free-air calculations. These grids were combined with the wind-tunnel grids for a given angle of attack by rotating and translating

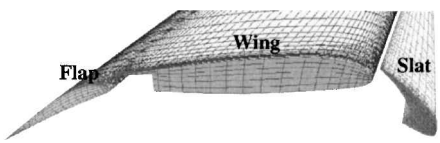

Fig. 3 Wing-cap grids on slat, wing, and flap.

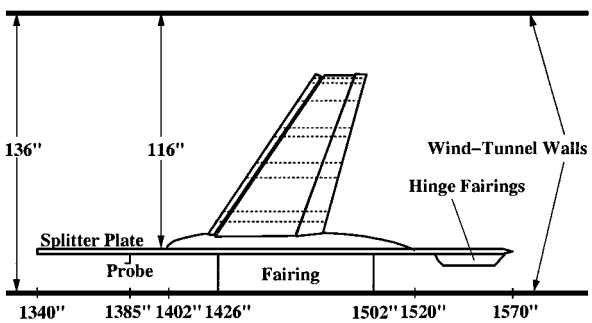

Fig. 4 Schematic view of trap wing inside 12-ft tunnel.

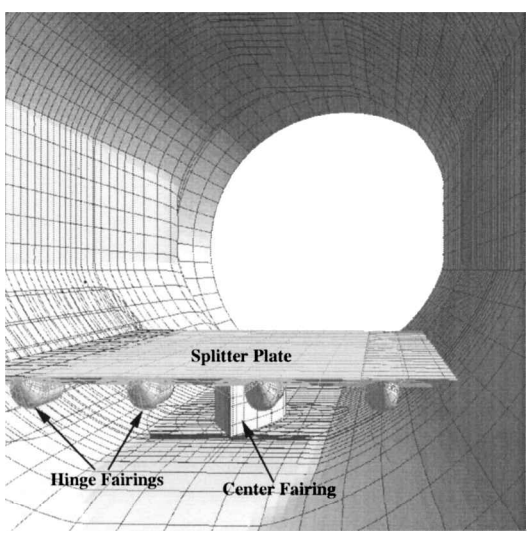

Fig. 5 Complete computational model of 12-ft tunnel test section.

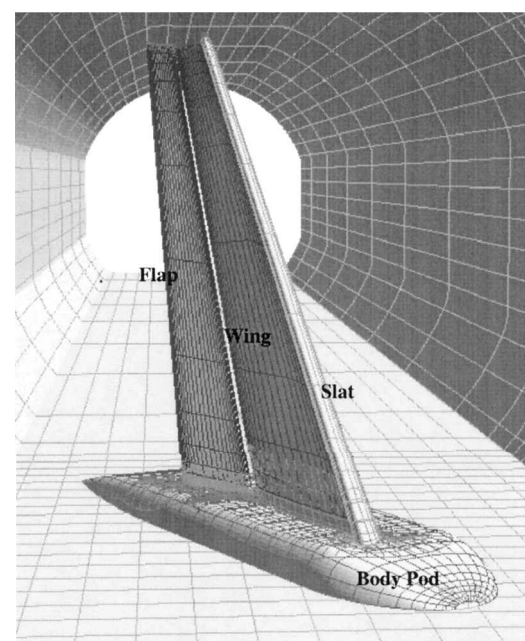

Fig. 6 Trap-wing surface grids inside simplified model of the 12-ft tunnel.

the wind-tunnel grids into the coordinate system of the trap wing. Use of the same coordinate system for all angles of attack simplified the postprocessing of the computed solutions.

Wind-Tunnel Boundary Conditions

One of the biggest challenges of using the viscous wind-tunnel model was determining the appropriate boundary conditions for the tunnel inflow and outflow, which would reproduce the same Reynolds and Mach numbers as the experiment. For the inviscid model this was straightforward: at the inflow boundary the total pressure and total temperature were specified to match the experimental values, and the other flow quantities were extrapolated from the neighboring downstream plane; at the outflow boundary the velocity magnitude was specified to match the mass-flow rate from the experiment, and pressure and density were extrapolated from upstream. This reproduced the same Mach and Reynolds number conditions as in the experiment.

The viscous model of the test section utilized the same total pressure and total temperature inflow conditions as the inviscid model. The boundary layer on the wind-tunnel walls in the viscous model precluded the use of a constant uniform velocity at the outflow. Another method was needed to control the mass flow through the tunnel. An "empty," viscous-tunnel grid system was used to develop an appropriate outflow boundary. This grid system was composed of the same viscous wind-tunnel grids but without the trap-wing grids embedded within the test section. Utilizing an outflow boundary condition, which specified the static pressure and extrapolated the other flow quantities, it was found that the mass flow could be adjusted by changing the value for the outflow static pressure. However, the appropriate value to use was not known a priori, as it was a function of the viscous losses in the wind tunnel and the drag force on the test article. In addition, much like in a real wind tunnel, it had to be determined how to sample the computed flowfield to evaluate the effective freestream reference conditions with the trap wing in place.

This issue was solved using a procedure analogous to the control system inside the 12-ft tunnel in a semispan testing mode. This approach interpolates flow quantities from the flowfield at six locations. Four of these are known as the Q-ring in the 12-ft tunnel and are located upstream of the test section, 128 in. (325 cm) upstream of the leading edge of the splitter plate. Two more probes sample the flow underneath the splitter plate, 46 in. (117 cm) downstream of its leading edge (see Fig. 4). The Mach numbers at these probe locations are used in a formula to compute the reference Mach number. The formula is based on the cross-sectional areas of the tunnel at the Q-ring, below the splitter plate and above the splitter plate. The formula used in the CFD was generated by integrating these areas from the actual CFD grid surfaces and was adjusted slightly with some calibration computations. The formula is

$$M_{\text{ref}} = 1.120 \times M_q + 0.0985 \times M_{\text{sp}}$$

where M_q is the average of the Mach numbers at the four Q-ring locations and where M_{sp} is the average of the Mach numbers at the two locations beneath the splitter plate. The calibration was performed by running the viscous-tunnel-only grid system for a number of different outflow static pressure ratios. The results of these calibration runs are plotted in Fig. 7. This figure plots M_q, M_{sp}, and the Mach number at the actual model reference location. It compares these with the reference Mach number computed with the preceding formula. As can be seen in Fig. 7, the measured and computed reference Mach numbers agree very well.

Thus, in order to compute a flow solution using the viscous model of the 12-ft tunnel test section the outflow static pressure must be iteratively adjusted until the desired reference Mach number has been obtained. In practice, the code was run for approximately 1000 cycles, until the mass flow through the tunnel had nearly converged. Then the reference Mach number was computed, and the outflow pressure boundary condition was adjusted. The code was then run for several hundred cycles until the rate of mass flow had once again nearly converged, and the adjustment was repeated. As seen in Fig. 7, the rate of change of Mach number with the outflow pressure is nearly linear within this low-speed range, and this process converged quickly. In practice, only four or five adjustments were needed to obtain the desired reference Mach number.

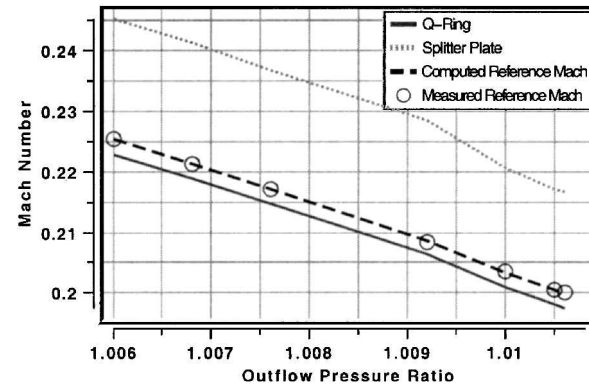

Fig. 7 Mach number vs outflow pressure.

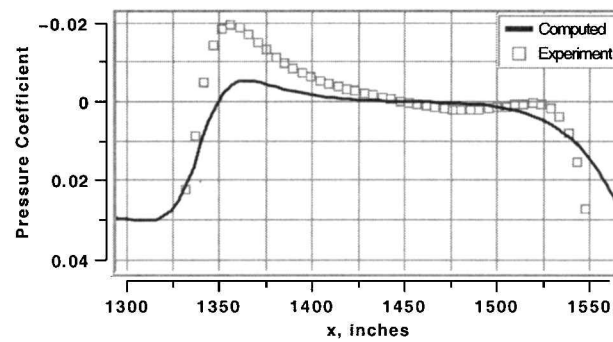

Fig. 8 C_p along the axis of the tunnel.

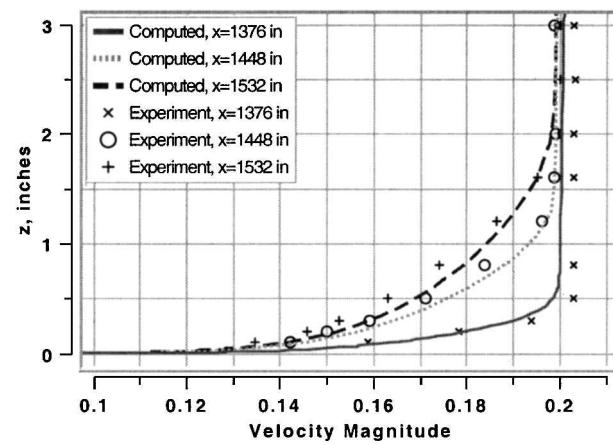

Fig. 9 Splitter-plate boundary layer in empty tunnel.

Some pressure-coefficient results from the empty viscous-tunnel calibration calculation are plotted in Fig. 8. This shows the pressure coefficient along an axial line 24 in. (61 cm) below the centerline of the tunnel. The experimental results were obtained during 12-ft tunnel calibration tests using a suspended static pipe with the semispan splitter plate and fairings installed. The experiment and calculations were run for a reference Mach number of 0.2 and a Reynolds number of 8×10^6/ft (26.3×10^6/m). The splitter plate leading edge is located at $x = 1340$ in. (3404 cm), and the trailing edge is located at $x = 1570$ in. (3988 cm). Figure 8 shows that there is very little variation in the pressure along the 19-ft (579-cm)-long plate, although the experimental result does show more acceleration at the plate leading edge than the computation and a slight deceleration through the middle of the test section. Figure 9 shows three boundary-layer profiles from both the computations and the experiment, above the splitter plate located at $x = 1376$, 1448, and 1532 in. (3495, 3678, and 3891 cm). The model reference location is at $x = 1448$ in. (3678 cm). Good agreement is seen between the computed and experimental

boundary layers, and the velocity profiles show more evidence of a slight deceleration in the experimental results.

Trap-Wing Flow Simulation and Analysis

Flow Solver

The OVERFLOW[4,5] Navier–Stokes flow solver was used in all of the current computations. This code is written to be efficient for computing very large-scale CFD problems on a wide range of supercomputer architectures. On vector supercomputers with very fast secondary memory devices, the OVERFLOW code includes an out-of-core memory management option, such that the total memory used is a function of the largest zone in the grid system, not the total number of grid points. The code is efficiently vectorized, and its multitasking directives take advantage of multiple processors. For cache-based multiple-processor machines the code has been parallelized with both a multilevel parallelism (MLP) library for shared memory systems, and with a message-passing interface library for nonshared memory systems. See Taft[26] (data also available on-line at http://www.nas.nasa.gov/Pubs/NASnews/98/01/overflow.html) and Jespersen[27] (data also available on-line at http://www.nas.nasa.gov/Pubs/TechReports/NASreports/NAS-98-013/) for more details. Most of the current cases were run with the standard OVERFLOW on a number of different single- and dual-processor Silicon Graphics Octane workstations, over a period of several weeks. Different angle-of-attack runs were run simultaneously on separate workstations. The code was run mostly during nonworking hours, utilizing computer resources that would otherwise have gone idle. The viscous-tunnel grid cases were too large to run on the Octane workstations; these cases were run on a Silicon Graphics Origin cluster at NASA Ames using the MLP version of OVERFLOW.

All of the OVERFLOW computations in the current work utilized the upwind-differencing scheme of Roe,[28] implemented with the van Leer monotone upstream-centered scheme for conservation laws third-order approach.[29] All of the computations also used the Spalart–Allmaras turbulence model[30] with the flow assumed to be fully turbulent. The viscous terms in all three directions are computed; however, the cross-derivative viscous terms were not included. These were not used because they add about 10% to the cost of the computation and because previous test cases have shown that their use does not affect the solution. The multigrid option[5] to the code was used with three levels. The current calculations also used the low-Mach-number preconditioning option[5] in the flow solver. The code was considered converged to a steady state when the L2 norm of the right-hand side had dropped at least two or three orders of magnitude for each computational grid and when the variation in the total lift coefficient was less than 0.01% over the last 100 cycles. Most cases required between 3000 and 6000 cycles to reach this convergence criteria and used between 360–720 h of SGI Octane CPU time for each of the inviscid wind-tunnel and free-air cases. The viscous wind-tunnel cases, which had twice as many grid points and required more cycles to converge, required approximately 1500 h of SGI Octane CPU time each.

Computed Results

The simulation conditions for the current analysis had a freestream Mach number of 0.15, a total pressure of 4.3 atm, and $Re_c = 14.7 \times 10^6$. The viscous wind-tunnel grid system was run for only two cases: 20 and 26 deg angle of attack. The inviscid wind-tunnel grids were run for 10 different angles of attack, ranging from −4 to 28 deg. Ten different angle-of-attack cases were run using free-air boundary conditions, ranging from −4 to 32 deg. Figure 10 shows C_L vs α for these computed results and for the corrected and uncorrected 12-ft tunnel experimental data. Figure 11 plots the drag coefficient C_D vs C_L for these same cases. These figures show that the viscous and inviscid grid systems produce the same lift and drag at 20 and 26 deg angle of attack. Also, it can be seen that both the wind-tunnel and free-air calculations agree very well with the uncorrected and the corrected experimental data at the lower angles of attack. Both the wind-tunnel and free-air computations predict $C_{L,\max}$ 3% lower than the corresponding experimental data. The predictions of the free-air model appear to agree with the corrected data as well as the wind-tunnel cases do with the uncorrected experimental data.

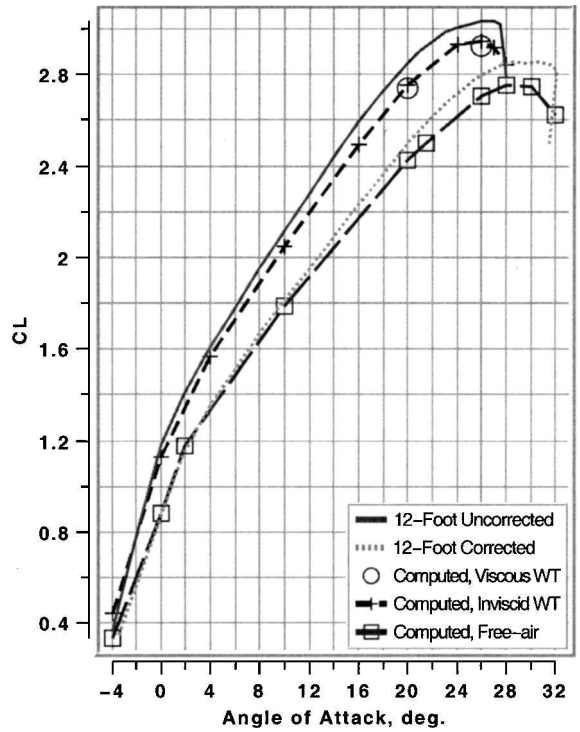

Fig. 10 C_L vs α.

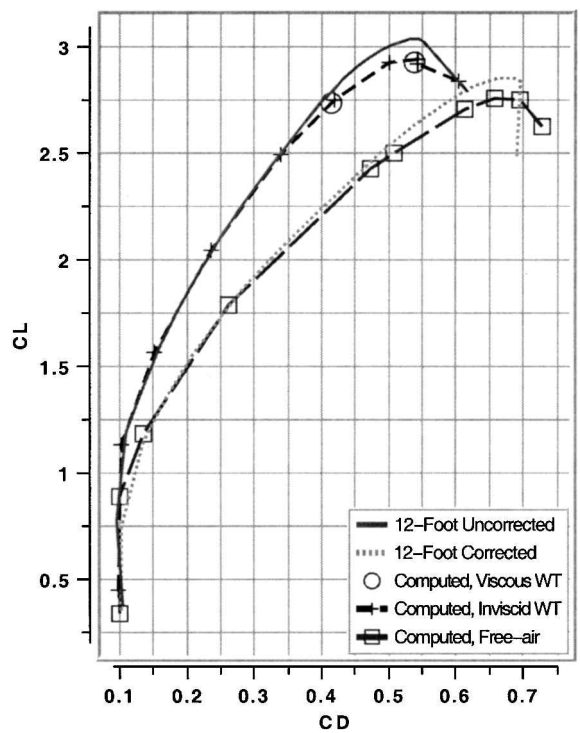

Fig. 11 C_L vs C_D.

Computational pressure data were extracted for comparison with experimental data from nine constant-span rows. These rows are denoted in Fig. 4 as dashed lines. These pressure-data rows are located at 17, 28, 41, 50, 65, 70, 85, 95, and 98% of the semispan of the wing.

Figures 12 and 13 show a comparison of uncorrected experimental surface pressure coefficients C_p with that from the computational cases using both viscous and inviscid wind-tunnel configurations at $\alpha = 20$ and 26 deg. The viscous-tunnel results are plotted with a solid line, and the inviscid tunnel results are plotted with a dashed line; however the results are so similar that the two sets of lines are

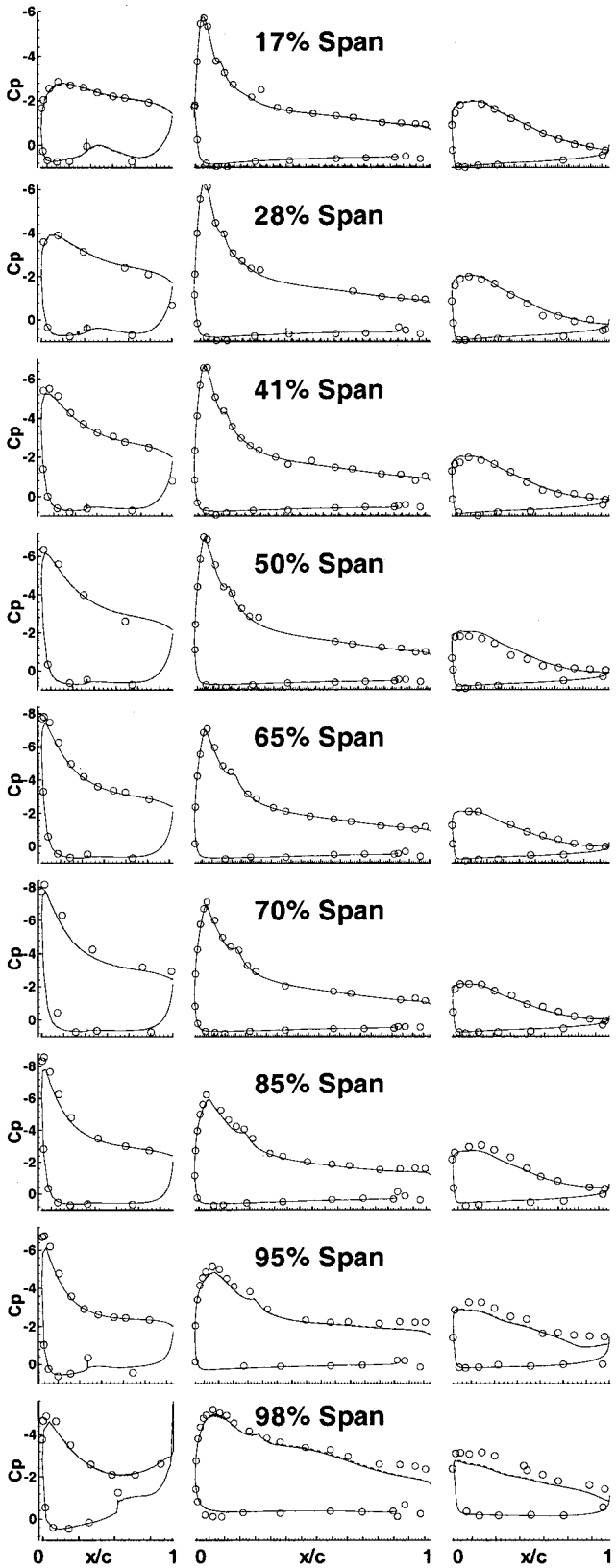

Fig. 12 C_p at $\alpha = 20$ deg: ——, viscous-tunnel calculations; – – –, inviscid-tunnel calculations; and o, experiment.

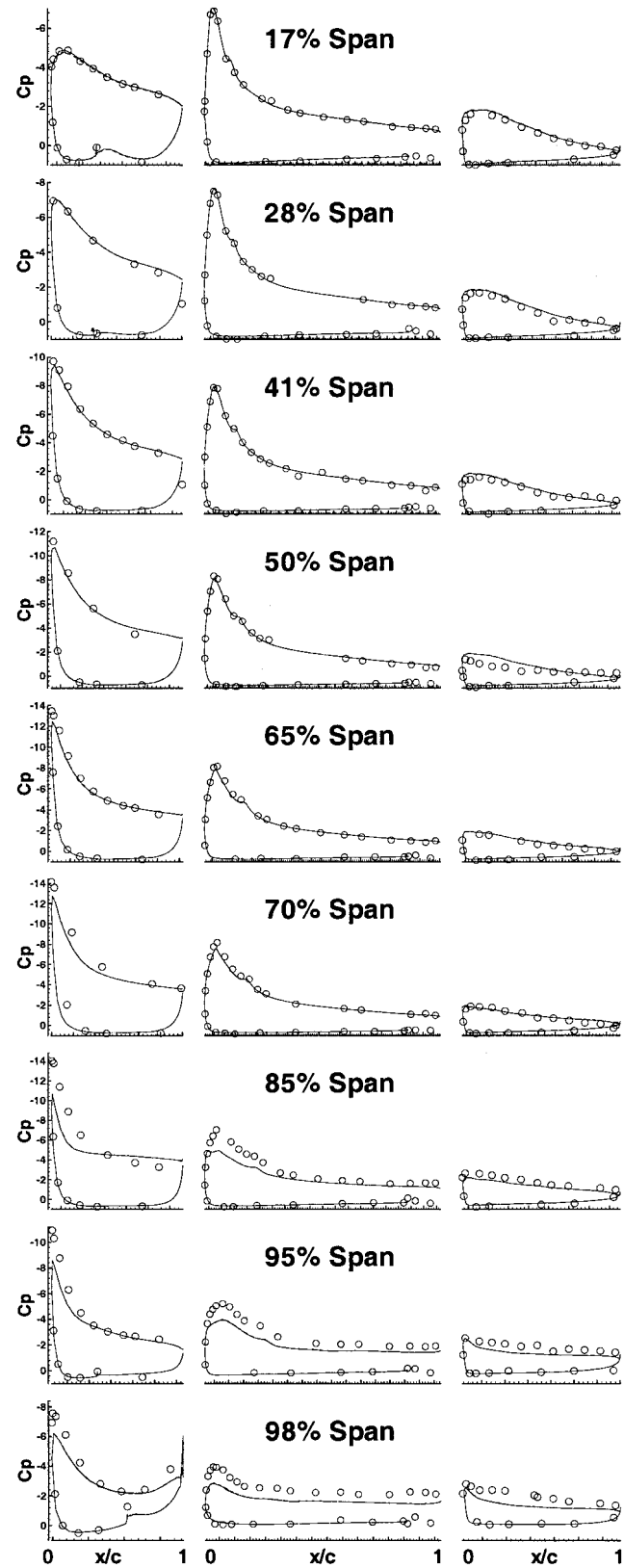

Fig. 13 C_p at $\alpha = 26$ deg: ——, viscous-tunnel calculations; – – –, inviscid-tunnel calculations; and o, experiment.

indistinguishable from each other. The agreement between the experimental data and the computational C_p is very good, especially at $\alpha = 20$. The computed results are producing less lift on the outboard region of the wing, particularly at $\alpha = 26$. Thus, the lower computed lift near $C_{L,\max}$ appears to be caused by a loss of lift at the outboard portion of the wing.

Examination of the $\alpha = 26$ inviscid-tunnel solution at the wing tip reveals a large vortex, starting at the slat edge, which convects and bursts over the top of the wing. This is shown in Fig. 14, which plots Mach-number contours and particle traces released at the slat edge. The Mach contours are drawn for values in the range between 0.0 and 0.1 and thus identify slow-moving fluid. The computed vortex spreads very rapidly as it passes over the wing, reducing the lift generated by the outboard portion of the wing. The grid resolution in the surface-normal direction has been refined enough to resolve the slat wake, but is not fine enough to properly resolve this slat-tip

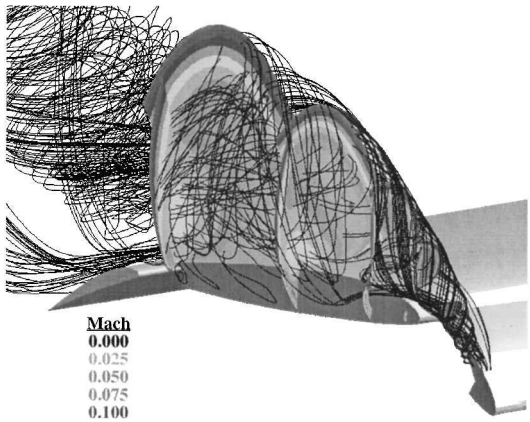

Fig. 14 Mach contours and particle traces; $\alpha = 26$.

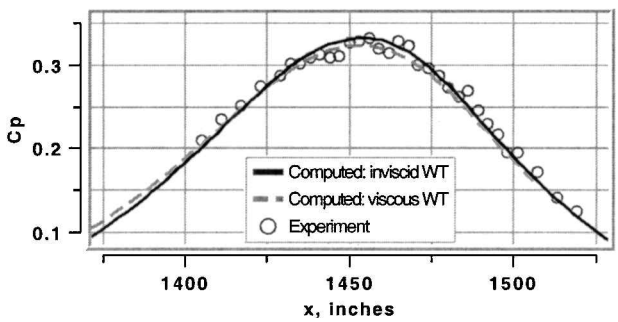

a) Pressure side

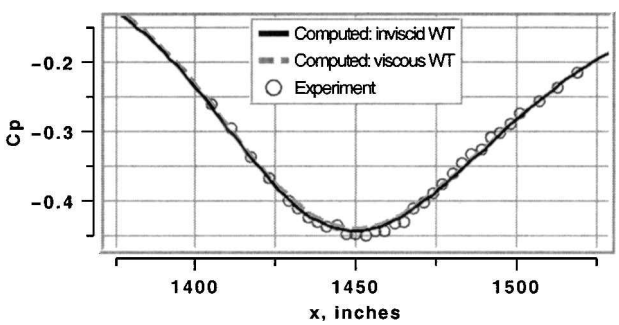

b) Suction side

Fig. 15 Wind-tunnel wall C_p at $\alpha = 26$.

vortex. The spanwise resolution in this region is also inadequate for this purpose. Thus, to better predict $C_{L,\max}$, the grid in this region probably needs to be refined.

Figure 15 shows a comparison of the C_p data on the side wind-tunnel walls (above and below the semispan wing) from the inviscid-tunnel computations, the viscous-tunnel computations, and the experiment, for the 26-deg angle-of-attack cases. The data are taken from the wind-tunnel walls at the 32% constant-span plane of the model. The results from the wall adjacent to the pressure side of the wing are plotted in Fig. 15a, and the suction-side wall results are shown in Fig. 15b. Very little difference is seen between the two computational results, and they both agree very well with the experimental data.

Wind Tunnel vs Free Air

After running all of the inviscid wind-tunnel cases, an attempt was made to compute a free-air case with the same lift as one of the higher angle-of-attack wind-tunnel cases. This was done to enable a comparison of local flow quantities and thus ascertain how effective a global angle-of-attack change is for providing wind-tunnel corrections. The inviscid wind-tunnel case at $\alpha = 16$ deg, with a lift coefficient of 2.493, was chosen. The free-air lift curve in Fig. 10 intersects this lift level at $\alpha = 21.46$ deg. This free-air case was computed, and the resulting lift coefficient was 2.502, only 0.4% higher. The resulting surface pressures are plotted in Fig. 16 using dashed

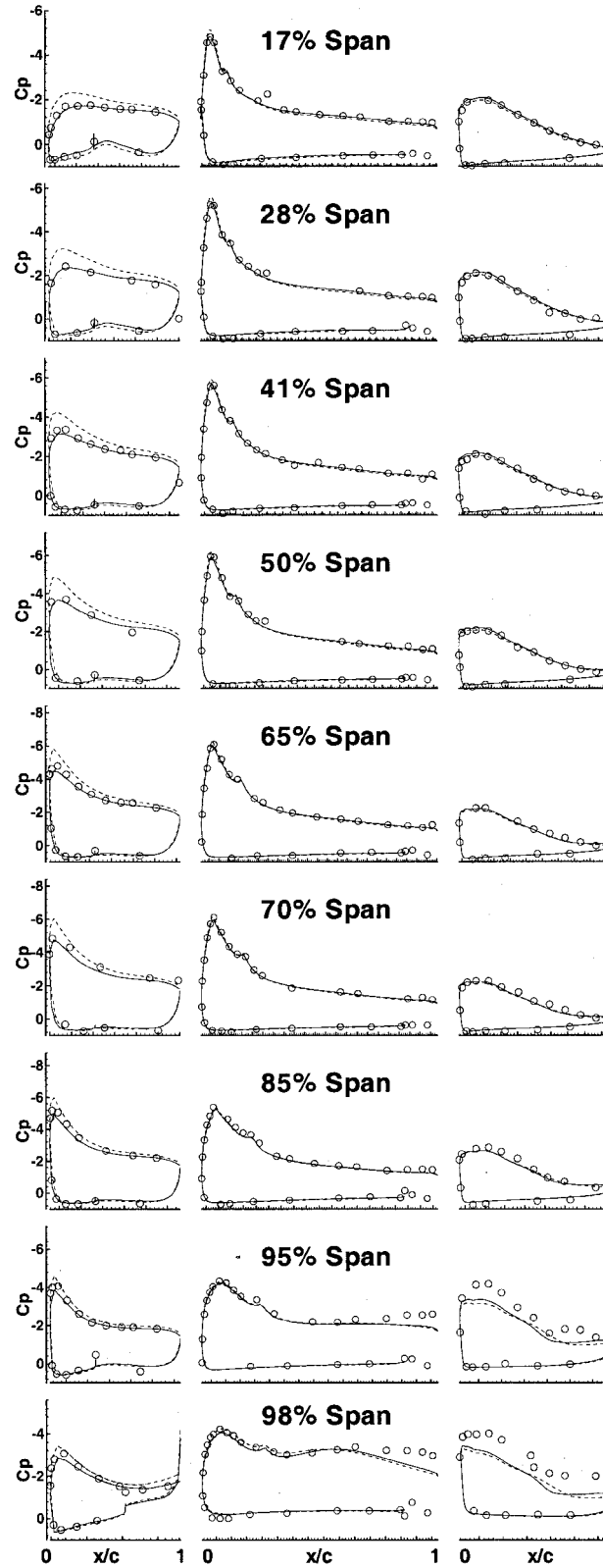

Fig. 16 C_p for wind tunnel and free air at $C_L = 2.5$; ——, inviscid wind-tunnel calculations, $\alpha = 16$; – – –, free-air calculations, $\alpha = 21.46$; and o, experiment, $\alpha = 16$.

lines. Also included in Fig. 16 are the experimental data (circles) and the inviscid wind-tunnel computational data (solid lines) from $\alpha = 16$ deg. It can be seen that there are significant differences between the two computed cases. The free-air data show more suction on the slat upper surface and thus more lift being generated on the slat. This results in a higher suction peak on the wing leading edge and also more downwash on the wing, which in turn results in less lift on the wing and flap.

Thus, a global correction to the angle of attack applied to a free-air calculation can result in the same integrated force quantities, such as lift, as computed in a wind-tunnel calculation. But the local flow quantities between the two cases may differ enough to change the relative loading of the wing elements. The conclusion is that it is always preferable to use a model of the wind tunnel, and not free-air boundary conditions, when utilizing experimental trap-wing data from the 12-ft tunnel.

Grid Refinement

The next step toward validation is to understand the differences between the experimental and computational results at maximum-lift conditions. The differences in C_p and the presence of the large slat-tip vortex at $\alpha = 26$ deg indicate that the spanwise grid resolution is probably not adequate outboard. To test this hypothesis, a new grid system was generated by adding 50% more spanwise grid points to the wing, slat, and flap. These new grid points were all added outboard of the 75% spanwise plane. Also, additional chordwise grid points were added to the slat to improve the resolution of the formation of the slat-tip vortex. The refined grid system was generated using the inviscid model of the wind tunnel and contained 8.7 million grid points.

Solutions were computed using this new grid system for several angles of attack. The resulting lift coefficients are plotted in Fig. 17, with the results from the original inviscid wind-tunnel grid system and the experimental results. At low angles of attack, the refined-grid results showed no change in the computed forces compared with the original computed data. However, distinct changes occur in the vicinity of maximum lift. The refined grid $C_{L,\max}$ is about 0.2 higher and occurs at an angle of attack that is about 4 deg beyond both the earlier computation and the experiment.

Figure 18 plots the surface C_p comparing the new-grid results (solid lines) with the old-grid results (dashed lines) and the experimental data (circles) for $\alpha = 26$ deg. The largest changes in the flow are near the wing tip, as expected. The new grid C_p shows excellent agreement with the experiment; this grid refinement has clearly improved the computational results outboard. Close examination of the upper surfaces indicates slightly lower pressures in the new solution across the entire span, which is evidence of the higher lift generated in the new solution. Even though the these surface pressures show better agreement with experiment than before, the refined grid is no closer to accurately predicting $C_{L,\max}$. This indicates that examination of the surface pressures alone is not enough to validate the computational ability to predict $C_{L,\max}$ and that doing so is dependent on the accuracy of the off-body viscous flow phenomena.

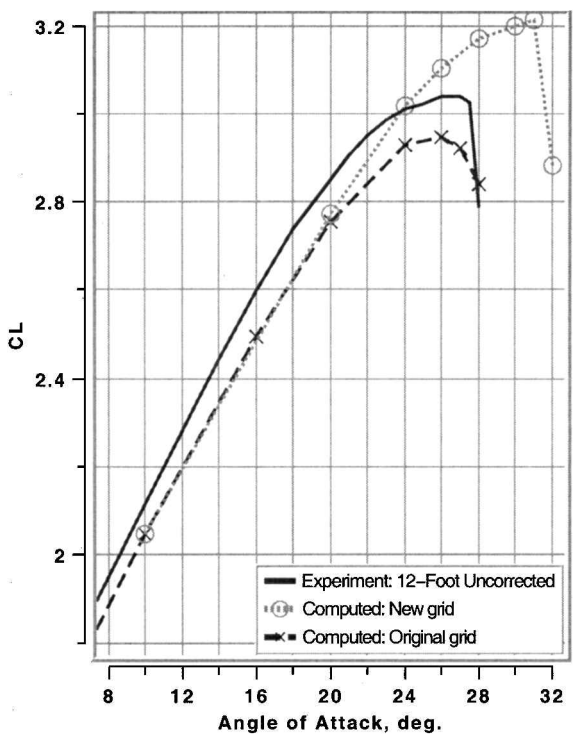

Fig. 17 C_L vs α.

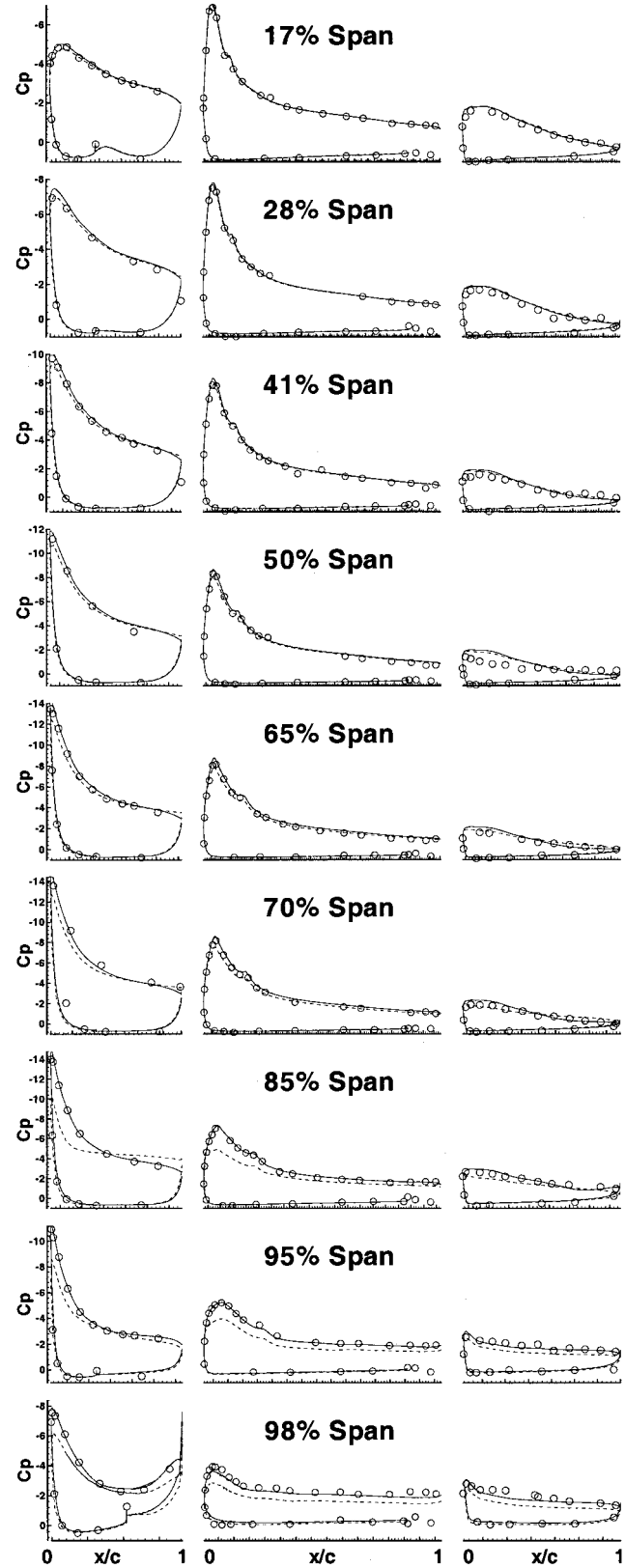

Fig. 18 C_p at $\alpha = 26$; ——, new grid; – – –, old grid; and o, experiment.

Summary

Results from an attempt to validate an overset-grid approach and the OVERFLOW solver for flow over a high-lift trapezoidal wing have been presented. Computations were performed using free-air

boundary conditions, a high-fidelity viscous model of the NASA Ames 12-ft Pressure Wind Tunnel, and a simplified, inviscid model of this wind tunnel. Only very minor differences were found between the two versions of the wind-tunnel simulations. The agreement between the computational and experimental lift and surface pressures are very good at lower angles of attack and not quite as good at higher angles of attack. The computed maximum lift was 3% lower than the experimental maximum lift. Investigation into the refinement of the grid system in the spanwise direction and of the slat chordwise spacing has led to improved predictions of the surface pressures at $\alpha = 26$ deg and also resulted in a computed $C_{L,\max}$, which was 5% higher than the experimental data.

The data presented here show a significant amount of evidence that the inviscid-tunnel approach is as accurate at simulating the wind-tunnel interference as the significantly more complex (and more computationally expensive) viscous-tunnel approach. Comparison of the pressure coefficients from free-air and inviscid-tunnel computations at the same lift conditions indicate that it is necessary to model the tunnel in order to compare local flow quantities with the 12-ft tunnel experimental data.

The results of the grid-refinement study indicate that not all grid sensitivities have been removed. Additional grid-refinement studies are warranted in the future. Once it has been determined that a grid-independent solution has been obtained, it would be possible to continue the validation effort by studying the effects of the modeling of transition, turbulence, and unsteady flow on the ability to compute $C_{L,\max}$. Additional assessments of the ability to predict Reynolds-number effects and the effects of flap and slat rigging changes could be performed by comparing with other configurations and conditions tested in the 12-ft tunnel.

Despite the questions arising near maximum lift, this work has accomplished its intended goals. The results have demonstrated that the presence of the wind-tunnel walls impacts the flow, and for the most accurate simulation the facility must be included in the computational model. It has been demonstrated that the current CFD approach can predict accurate forces and surface pressures at low to moderate angles of attack.

Acknowledgments

This work was partially funded by the Advanced Subsonic Technology Program through NASA Contract NAS2-20268. The authors gratefully acknowledge the technical help of Pieter Buning and Kenneth Jones of NASA Langley Research Center; M. David Baker, Michael Olsen, and Mike Madson of NASA Ames Research Center; and Paul Johnson of the Boeing Company. They also wish to acknowledge the helpful comments from Lyndell King and Cetin Kiris of NASA Ames Research Center in their review of this work.

References

[1]Benek, J. A., Buning, P. G., and Steger, J. L., "A 3-D Chimera Grid Embedding Technique," AIAA Paper 85-1523, July 1985.

[2]Rogers, S. E., Cao, H. V., and Su, T. Y., "Grid Generation for Complex High-Lift Configurations," AIAA Paper 98-3011, June 1998.

[3]Rogers, S. E., Roth, K., Nash, S. M., Baker, M. D., Slotnick, J. P., Cao, H. V., and Whitlock, M., "Advances in Overset CFD Processes Applied to Subsonic High-Lift Aircraft," AIAA Paper 2000-4216, Aug. 2000.

[4]Buning, P. G., Jespersen, D. C., Pulliam, T. H., Chan, W. M., Slotnick, J. P., Krist, S. E., and Renze, K. J., "OVERFLOW User's Manual, Version 1.8b," NASA Langley Research Center, Hampton, VA, 1998.

[5]Jespersen, D. J., Pulliam, T. H., and Buning, P. G., "Recent Enhancements to OVERFLOW," AIAA Paper 97-0644, Jan. 1997.

[6]Lynch, F. T., Potter, R. C., and Spaid, F. W., "Requirements for Effective High Lift CFD," *20th Congress of the International Council of the Aeronautical Sciences Proceedings*, Vol. 1, AIAA, Reston, VA, 1996, pp. 1479–1492.

[7]Meredith, P. T., "Viscous Phenomena Affecting High-Lift Systems and Suggestions for Future CFD Development," *High-Lift System Aerodynamics*, CP-515, AGARD, 1993, pp. 19.1–19.8.

[8]Bussoletti, J., Johnson, P., Jones, K., Roth, K., Slotnick, J. P., Ying, S., and Rogers, S. E., "The Role of Applied CFD Within the AST/IWD Program High-Lift Subelement: Applications and Requirements," AST/IWD Program Rept., NASA Langley Research Center, Hampton, VA, June 1996.

[9]Mathias, D. L., Roth, K., Ross, J. C., Rogers, S. E., and Cummings, R. M., "Navier–Stokes Analysis of the Flow About a Flap-Edge," AIAA Paper 95-0185, Jan. 1995.

[10]Jones, K. M., Biedron, R. T., and Whitlock, M., "Application of a Navier–Stokes Solver to the Analysis of Multielement Airfoils and Wings Using Multizonal Grid Techniques," AIAA Paper 95-1855, June 1995.

[11]Cao, H. V., Rogers, S. E., and Su, T. Y., "Navier–Stokes Analyses of a 747 High-Lift Configuration," AIAA Paper 98-2623, June 1998.

[12]Mavriplis, D. J., "Large-Scale Parallel Unstructured Mesh Computations for 3D High-Lift Analysis," AIAA Paper 99-0537, Jan. 1999.

[13]Mavriplis, D. J., "Three-Dimensional Viscous Flow Analysis for High-Lift Configurations Using a Parallel Unstructured Multigrid Solver," Society of Automotive Engineers, Paper 1999-01-5558, Oct. 1999.

[14]Nash, S. M., and Rogers, S. E., "Numerical Study of a Trapezoidal Wing High-Lift Configuration," Society of Automotive Engineers, Paper 1999-01-5559, Oct. 1999.

[15]Slotnick, J. P., An, M. Y., Mysko, S. J., Yeh, D. T., Rogers, S. E., Roth, K., Baker, M. D., and Nash, S. M., "Navier–Stokes Analysis of a High-Wing Transport High-Lift Configuration with Externally Blown Flaps," AIAA Paper 2000-4219, Aug. 2000.

[16]Rogers, S. E., Roth, K., Slotnick, J. P., Cao, H. V., Whitlock, M., Nash, S. M., and Baker, M. D., "Computation of Viscous Flow For a Boeing 777 Aircraft in Landing Configuration," AIAA Paper 2000-4221, Aug. 2000.

[17]Johnson, P., Jones, K. M., and Madson, M., "Experimental Investigation of a Simplified 3D High Lift Configuration in Support of CFD Validation," AIAA Paper 2000-4217, Aug. 2000.

[18]King, L. S., and Johnson, D. A., "Transonic Airfoil Calculations Including Wind Tunnel Wall-Interference Effects," *AIAA Journal*, Vol. 24, No. 8, 1986, pp. 1378–1380.

[19]Beutner, T. J., "A Method for the Modelling of Porous and Solid Wind Tunnel Walls in Computational Fluid Dynamics Codes," Ph.D. Dissertation, Dept. of Aeronautics and Astronautics, Stanford Univ., Stanford, CA, Dec. 1993.

[20]Martin, F. W., Sickles, W. L., and Stanley, S. A., "Transonic Wind Tunnel Wall Interference Analysis for the Space Shuttle Launch Vehicle," AIAA Paper 93-0420, Jan. 1993.

[21]Vatsa, V. N., and Wedan, B. W., "Navier–Stokes Solutions for Transonic Flow over a Wing Mounted in a Tunnel," AIAA Paper 88-0102, Jan. 1988.

[22]Cao, H. V., Kusunose, K., Spalart, P., Ishimitsu, K., Rogers, S. E., and McGhee, R., "Study of Wind Tunnel Wall Interference for Multi-Element Airfoils Using a Navier–Stokes Code," AIAA Paper 94-1933, June 1994.

[23]Djomehri, M. J., "CFD Modeling of the 12-Foot Pressure Wind Tunnel," Calspan, Internal Rept., NASA Ames Research Center, Moffett Field, CA, April 1996.

[24]Chan, W. M., Rogers, S. E., Nash, S. M., and Buning, P. G., "Chimera Grid Tools, Version 1.1 User Guide," NASA Ames Research Center, Moffett Field, CA, Oct. 1998.

[25]Parks, S. J., Buning, P. G., Steger, J. L., and Chan, W. M., "Collar Grids for Intersecting Geometric Components Within the Chimera Overlapped Grid Scheme," AIAA Paper 91-1587, July 1991.

[26]Taft, J., "OVERFLOW Gets Excellent Results on SGI Origin2000," *NAS News*, Vol. 3, No. 1, 1998, pp. 1–3.

[27]Jespersen, D. J., "Parallelism and OVERFLOW," NASA Advanced Supercomputing Facility, TR NAS-98-013, NASA Ames Research Center, Moffett Field, CA, Oct. 1998.

[28]Roe, P. L., "Approximate Riemann Solvers, Parameter Vectors, and Difference Schemes," *Journal of Computational Physics*, Vol. 43, No. 3, 1981, pp. 357–372.

[29]Anderson, W. K., Thomas, J. L., and van Leer, B., "A Comparison of Finite Volume Flux Vector Splittings for the Euler Equations," *AIAA Journal*, Vol. 24, No. 9, 1986, pp. 1453–1460.

[30]Spalart, P. R., and Allmaras, S. R., "A One-Equation Turbulence Model for Aerodynamic Flows," AIAA Paper 92-0439, Jan. 1992.

S. K. Aggarwal
Associate Editor